Silicon
https://doi.org/10.1007/s12633-024-02997-8

RESEARCH

Synthesis of Novel [$CdO_{(75\%)}/VO_{2(20\%)}/SiC_{(4\%)}$:p-Si] Heterojunction Composite Thin Films Decorated with Chlorophyll using Solvothermal-Laser Dual Technique for Solar Cell Applications

Ammar Abd Ali Najm[1] · Saif M. Alshrefi[2] · Zaid L. Hadi[1] · Ehssan Al-Bermany[3] · Ameen Alwan Mohaimeed[1,4]

Received: 28 January 2024 / Accepted: 14 April 2024

Abstract
The solvothermal technique is utilized to deposit the nanoparticles into nano-thin films. Where Vanadium dioxide (20%) was mixed with (4%) of SiC, then added to CdO with (75%) to fabricated nanocomposites. PLD technique used Nd: YAG laser with a different energy to deposit nano-thin films on p-Si substrate to get [$CdO_{(75\%)}/VO_{(20\%)}/SiC_{(4\%)}$: p − Si]. Scanning electron microscope (SEM) revealed the expected behavior of grain formation, with granules evenly dispersed across the film surfaces of CdO, VO_2, and SiC at particular places. In the presence of increased laser energy, the particle size decreases from 61 to 52 nm recognized. Elemental abundances of Cd, V, Si, C, O, and Mg were determined by energy dispersive X-ray analysis (EDX) to be relatively high. XRD revealed a polycrystalline structure with discriminatory orientations in planes (100) and (101); the peaks of SiC at (111) and (220) appeared at angles ($2\theta = 34.1°$, and 60°), respectively. The diffraction angle ($2\theta = 34.1°$) was observed for Mg at level (111). By increasing laser pulsing, the optical absorption of the prepared composite increases from 310 nm of S1 to 330 nm of S2 and displays blue, and the band gap energies are reduced from 2.7 eV of S1 to 2.5 eV of S2. According to the current–voltage heterojunction characteristics, the forward bias current changes rapidly with applied voltage in the dark, consistent with the tunneling-recombination model. The I-V characteristics curve presented the efficiency of synthesizing nanocomposite thin film in a solar cell is $\eta = 11$ with $FF = 0.48$ under illumination.

Keywords CdO · VO_2 · SiC · Chlorophyll · Solvothermal · PLD · Nanocomposites · Optical Properties

1 Introduction

Nanoparticles (NPs) have a large surface-to-volume ratio, making them useful in physics, chemistry, engineering, and biology [1, 2]. Nanomaterials can be classified as 0D, 2D, and 3D, depending on their dimensions. As nanoparticles are either crystalline or amorphous, they are composed of both phases. There are numerous different shapes for nanomaterials, including cubes, fibers, films, wires, and plates [3–8]. Nanoparticles are produced through chemical and physical methods, according to procedure grinding, lithography, ion ejection, and laser ablation [9, 10]. Alternatively, chemical methods include sol–gel, thermal decomposition, salt reduction, reverse micelles, hydrothermal, and co-precipitation [11, 12]. Several researchers have reported that transition metal oxides can be synthesized as nanoparticles, and their properties are characterized and applied [13]. Because of their simple crystal structures, significant carrier mobility, and sometimes near-metallic conductivities [14], CdO-based transparent conductive oxides are noteworthy. CdO, an n-type semiconductor in bulk form, has a high direct band gap of 2.27 eV and a tiny indirect band gap of 0.55 eV. Cadmium and oxygen vacancies determine the band gap to a large extent, depending on the synthesis procedures [15]. According to the Refractive index, cadmium oxide has a remarkable value ($n = 2.49$), which makes it an attractive substrate for optoelectronics applications. The solvothermal technique employs CdO crystals that can be synthesized

✉ Ehssan Al-Bermany
ehssan@uobabylon.edu.iq

1 General Directorate of Education in Babel Governorate, Babil, Iraq

2 Laser Physics Department, College of Science for Women, University of Babylon, Babil, Iraq

3 Department of Physics, College of Education for Pure Science, University of Babylon, Babil, Iraq

4 Medical Physics Department, College of Sciences, Al-Mustaqbal University, 51001 Babil, Iraq

Published online: 22 April 2024

directly from solutions. Different synthesis conditions result in crystals of varying shapes, sizes, and structures [16].

A semiconductor–metal phase transition (SMPT) has been observed in vanadium dioxide VO_2 at ambient temperature. A range of polymorphic structures are particularly suitable for various applications. A first-order reversible metal–insulator transition occurs at T_c 68° C (341° K). Consequently, this material can be used as a thermos Ensor, a thermo-switch, an optical switcher, shutters, IR sensors, thermochromic coatings, and so on [17, 18]. An example of a device that may convert solar radiation into heat and transfer that heat to the working fluid through its surface is called a solar receptor. The materials used for fabrication must be capable of withstanding high levels of radiative flow and mechanical stress for many hours without breaking. Its characteristics are high absorbance, surface area, porosity, fusion point, and thermomechanical characteristics at high temperatures [19].

The use of SiC in solar receivers in central tower plants has excellent advantages, which contribute to the efficiency of the production of electrical energy [20, 21]. SiC exhibits a considerable amount of polymorphism, which impacts its mechanical properties, with a more extensive Young module than β-SiC (347 to 314 GPa) [20]. Solvent-based synthesis creates a wide range of materials, from metal oxides and semiconductors to ceramics and polymers. The method involves the application of a solvent at temperatures between 100 and 1000 degrees Celsius and pressures between 1 and 10 atmospheres. Allows more accessible precursor contact during the synthesis. Hydrothermal synthesis occurs when water is utilized as a solvent, commonly carried out at temperatures lower than the 374°C supercritical point of water. In this process, thin films, bulk powders, single crystals, and nanocrystals are all possible. A controlled crystal structure can be achieved by manipulating the solvent supersaturation, the chemical concentration, and the kinetics. Other methods cannot efficiently synthesize novel materials. Over 80% of the literature on solvothermal synthesis has been reported to focus on nanocrystal synthesis [22]. Due to this, a review examines recent advances in solvothermal synthesis, particularly nanocrystalline synthesis [23]. Utilizing the PLD technique, high-quality structures can be made from a wide variety of materials in an uncomplicated, quick, and inexpensive manner. Despite its limitations regarding the surface area covered, PLD is still gaining interest among researchers. High adherence of the deposited structures to the substrate and stoichiometric transfer of the target composition are further benefits. Besides the coating's phase, crystallinity and thickness were managed by adjusting the coating's morphology and chemical composition. There were also lower porosities and decreased cracking or delamination of the deposited structures [24]. It has been seen that chlorophyll is a natural green pigment that is crucial to human nutrition. Green vegetables need a high amount of chlorophyll due to their biological function.

Building using PLD is easy, fast, and cheap, allowing for the construction of high-quality structures from various materials. Chlorophyll displays antioxidant properties as well as antimutagenic and anticarcinogenic properties. Thus, chlorophyll and its derivatives have been the subject of studies focused on cancer prevention. The only organic semiconductors are chlorophylls from a precursor resource such as spinach or spirulina that are transferred to a solid-state device. Due to its photovoltaic properties, it is likely the shortest and lightest optoelectronic device of our time. As shown in Fig. 1, chlorophyll dye solar cells are commonly assembled in laboratories. The photosynthetic process produces a hole-electron pair in thin film devices (a) and (b). Chlorophylls are usually electron donors, although exceptions are possible, for enhancing the transport of

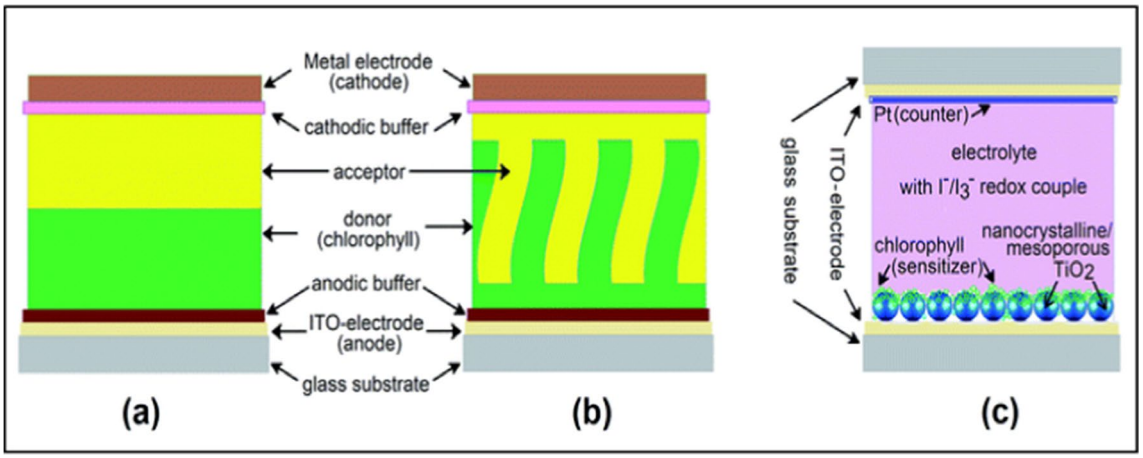

Fig. 1 Photovoltaic device schematic featuring (**a**) a planar heterojunction (PHJ) thin-film cell, (**b**) a bulk heterojunction (BHJ) thin-film cell, and (**c**) a dye-sensitized solar cell (DSSC) [29]

newly produced pigment molecules into sensitive materials for photosynthetic complexes [25]; through the process of photoionization, electrons acquire significant amounts of energy when light stimulates chlorophyll molecules, enabling them to break free from the chlorophyll and resulting in a positive charge for the chlorophyll. When some high-energy electrons return to the chlorophyll, the extra energy is rapidly released as heat or light, causing chlorophyll to appear fluorescent [26, 27]. Molecular pairs of donors and acceptors, such as p-type and n-type semiconductors, were created. Another organic semiconductor (acceptor) forms the second component of this junction [28, 29]. This research's main novelty is connecting the materials with dye as thin films with interstitial fluid (Extract Dye) deposited on Si-Wafer. In addition to fabricating new nanocomposites-thin films from Vanadium dioxide (20%) were mixed with (4%) of SiC, then added to CdO with (75%) using the PLD technique used Nd: YAG laser and the solvothermal technique for the first time.

2 Experimental Details

2.1 Preparation of Plant Samples for Methanol Extraction

Dactylon Cynodon is a prostrate, creeping plant with a stoloniferous root system and a rhizomatous root system. The leaves are grey-green, about 2 to 15 cm long, and 0.5 to 1 mm wide [19]. The Iraqi flora and taxonomic literature were used to choose plants from October to December 2017 in Hillah City. After gathering leaves, they were taken indoors, washed with running water to remove debris or bugs, chopped up, or shade-dried before being pulverized into a powder. Twenty grams of the ground-up leaf were given 24 h to absorb the methanol (MeOH) in a Soxhlet extractor. The chlorophyll extract dye was a dark green color and 300 mg/ml concentration after the solvent was filtered out and evaporated in an oven set to (50°C).

2.2 Sample Preparation

Sigma-Aldrich provided the following materials for the unprocessed synthesis of the nanostructures under investigation. [$CdO_{(75\%)}/VO_{2(20\%)}/SiC_{(4\%)}$] Nanostructures were formed on p-type silicon substrates utilizing a low-temperature aqueous chemical growth approach. For Step One, the substrates were sonicated for 20 min in an ultrasonic cleaner bath containing methanol, followed by an acetone wash and hydrogen gas drying. Chlorophyll dye was deposited on these substrates using the Spin-coater technique. This procedure was performed twice at 3000 rpm for 20 s, and the samples were annealed at around 90°C for 20 min. The next step is to dissolve 2 g of KOH in 10 ml of water, mixed with 0.5 g of SiC, grain size around 30–40 nm, and transfer to a 30 ml glass baker under continuous magnetic stirring. Next, prepare a stirred solution of 4 g of CdO dispersed in 15 g of water and 1.5 g of VO_2 dispersed in 10 g of water. Lastly, all the solutions were mixed and injected into the autoclave for 24 h at a temperature of 180 °C. To boost the encouraging oxides mixed with them, a piece of high-carbon steel was submerged into the Teflon Jar of the autoclave, as shown in Fig. 2. Once the autoclave has been switched off, it should be allowed to cool down to room temperature. In the following step, the product was extracted and washed with diluted water with ethanol, then dried at 60 °C for 24 h. Figure 3 depicts the process by which the powder and colloids were extracted from the resulting brown emulsion by filtering it through the aperture in a vacuum of 10^{-1} bar. Subsequently, the product required five rounds of washing, each with solutions of ethanol and water separately. After centrifugation, the suspension was dried and placed in an oven for two hours at around 100 °C. One hour of preheating at 80°C was performed on samples to produce nanostructures.

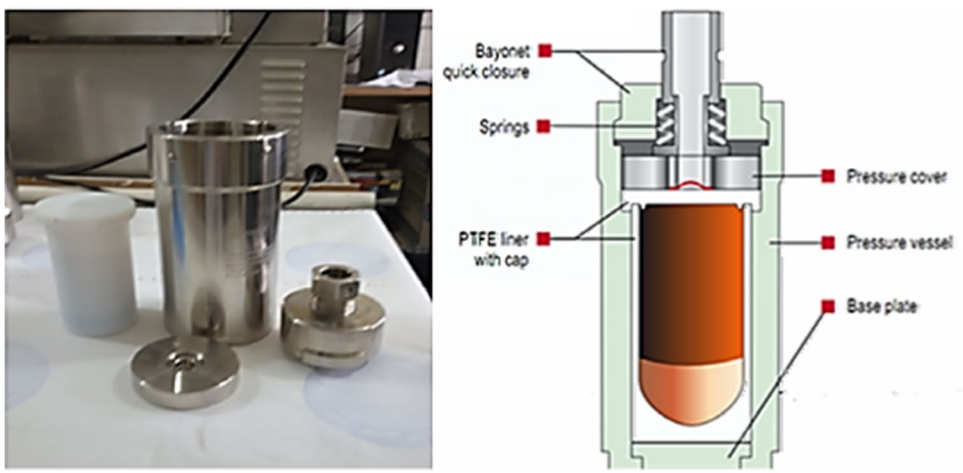

Fig. 2 Solvothermal system employed in the research

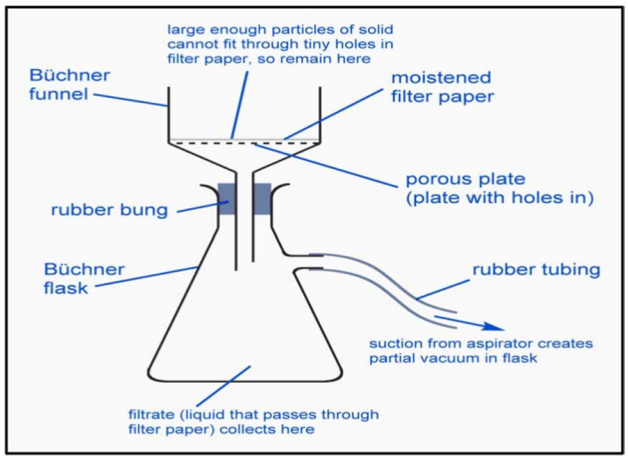

Fig. 3 Diagram of Laboratory Filtration System

A room-temperature air-drying process was then carried out on the pieces.

2.2.1 Laser Process

The Nd: YAG Laser system (MED-810, KES Biology Technology Co. Ltd.) with 1064 nm wavelength. A laser pulse energy of 80 mJ and a pulse duration of 10 ns was required to ensure a high-quality factor. Depending on the number of pulses 100 and 200 to deposit on the substrate of the p-silicon wafer. The deposited system is compact and controls key parameters by computer, such as the power and repetition rate. The PLD system has three major components: the vacuum chamber, pumps, and gauges. The PLD system prepared thin films at nanoscales. The set-up includes several parts, like a vacuum chamber, lens with a focal length of 30 cm, quartz window, Q-switching Nd: YAG laser, and the rotary pump, diffusion pump, Argon cylinder, and pressure monitor. The resulting research samples will be: S1 is $[CdO_{(75\%)}/VO_{2(20\%)}/SiC_{(4\%)} : p-Si]$ under 80mJ and 100 pulses, whereas S2 is within the same energy at 200 pulses.

3 Instruments

An optical interferometer is used as a tool for measuring thin film thickness. This technique uses interference fringes of a He: Ne laser (632.8 nm) operated at low power. The observation of the laser beam reflected by the thin film and the substrate away from their surfaces. Calculating the thickness using the formula in Eq. 1 [28] is possible.

$$t = \frac{y}{x} \times \frac{\lambda}{2} \tag{1}$$

In this equation, t represents the predicted thickness, y is the width and wavelength of the dark fringe, and x is the light fringe's width. Thin film samples S1 and S2 had calculated 308 nm and 280 nm thicknesses, respectively.

4 Results and Discussion

Different ions from the same precursor source affect the morphology of metal oxide nanostructures. As shown in Fig. 4, $[CdO_{(75\%)}/VO_{2(20\%)}/SiC_{(4\%)} : p-Si]$ nanostructures with nano-porous morphology formed on p-type silicon substrate display characteristic SEM images. Porous semicircular nanostructures have been effectively created in composites containing Cd, Mg, and K ions. Under heat and pressure, silicon carbide has a thermodynamic instability, and dehydration occurs, which is why SiC is an oxygen reducer. During the study of the effect of KOH on the Inner overlay of $[CdO_{(75\%)}/VO_{2(20\%)}/SiC_{(4\%)}]$ nanostructures, it was found that the general reaction of the solutions was towards vanadium oxide. Since the solvent medium is alcohol diluted with Distilled Water, several compounds were observed, such as Hydrous Potassium Hypo-Vanadate ($K_2V_4O_9$), Vanadium Oxysulfate $VOSO_4$ and Dipotassium Sulfate K_2SO_4. An excess of ten percent solution of caustic potash is added to a boiling solution of Vanadyl Salt without air. As in a chemical reaction, the result is cooled without air:

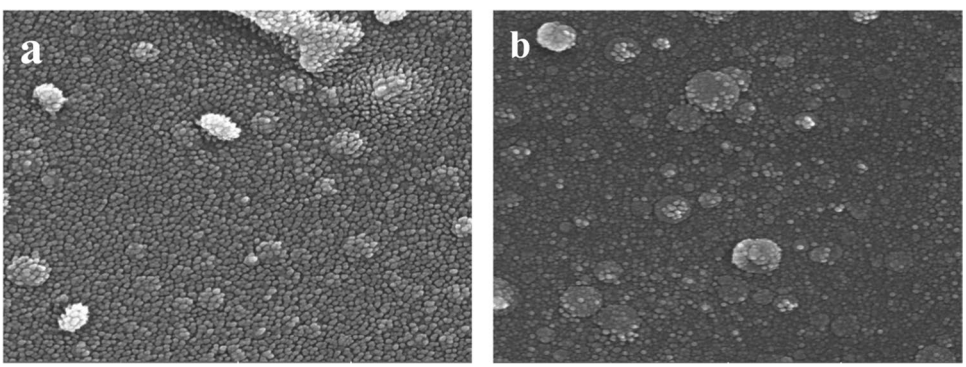

Fig. 4 SEM Images (**a**) S1 and (**b**) S2 samples

$$4\ VO_2 + 2\ KOH \rightarrow K_2V_4O_9 + H_2O$$

$$4\ VOSO_4 + 10\ KOH \rightarrow K_2V_4O_9 + 4K_2SO_4 + 5\ H_2O$$

Potassium Vanadinite ($K_2V_4O_9$) is a brown, pearly, glistening mass similar to ammonium salt [30]. In the form of amorphous powder, vanadium oxides V_2O_4 or VO_2 are shown as a dark green. Vanadyl salts are insoluble in water but soluble in sodium hydroxides, potassium hydroxides, and acids formed by vanadyl salts. A darkish brown crystal is formed from potassium hypo vanadate, which is soluble in water but almost insoluble in alcohol. Therefore, the output precipitation product is darkish brown or black [31]. In this instance, a network of nanoparticles was created, as shown in Fig. 4.

During sintering, nano-inclusions are effective in resisting grain growth. Reducing grain sizes also decreases thermal conductivity because of increased scattering at grain boundaries. From S1 to S2, the grain size decreases from 62 to 52 nm, as shown in Fig. 4b. The nanoparticle composites have a more uniform morphology because of the CdO reacting with the SiC nanoparticle composites. Hence, this behavior can be ascribed to the increasing number of pulses, which create short chemical bonds between the interfaces. As a result, the residues had a harmonious surface arrangement. This result led to a straightforward path for electrons generated by light interactions with the precipitate if later used as a solar cell, consistent with other research findings [32–34]. A particular interest is in producing monodisperse metal oxide nanoparticles of varying diameters. Furthermore, it provides superior electrical conductivity compared with other morphologies due to its increase in surface area [35, 36]. CdO is insoluble in water; CO_2 can be captured from the air and reduced into conducting oxides. It is one of the promising optoelectronic candidates [37]. Due to its properties, such as wide band gap, low electrical resistivity, and high transmission in the visible region, Cadmium oxide (CdO) can be used in a wide range of solar cells [38, 39]. Even though all SiC particles showed superficial sections, they had well-aligned granular morphology. Compact particles showed some deviations from the growth direction, as displayed in Fig. 4a. The surface of the thin film, as illustrated in Fig. 4b, covered the entire thickness at higher pulses. However, they were restricted to starfruit, which aligns with other researchers' findings [39–41]. The degradation of chlorophyll is a natural part of the life cycle of photosynthetic organisms. Chlorophyllase catalyzes this activity by hydrolyzing C-173 ester bonds with excellent stereospecificity. Polar products like Chlorophyllide-a exist in lipid environments to undergo different metabolic responses. To facilitate the transport of newly synthesized pigment molecules into the target photosynthetic complexes, reaction centers, and antennae. Therefore, the esterification of the C-173 carboxylic group with long-chain alcohol is necessary. In many of these photosynthetic complexes, chlorophyll interacts with the hydrophobic domains of apoproteins [42]. Therefore, The SEM images reveal composites, which are compact grains due to chlorophyll. They are assisting in the development of refined semi-spherical grains. Surface confinement generally decreases as laser pulses increase and grain size decreases the thin film layers interact with plasma ablation products and chlorophyll dye in this process. The result is a reduction in grain size and a purification process using more laser pulses after the reduction is complete [43]. Moreover, the composite was homogeneous with some surface pores, indicating that crystallites did not aggregate inside a particle, where particles are composed of many globular granules. Hence, Mg and C ions play essential roles in shaping $[CdO_{(75\%)}/VO_{2(20\%)}/SiC_{(4\%)}]$ nanostructures into a morphology similar to confinement grains. Other grains contained fewer twins and dislocations, whereas others had a high density of twins and stacking faults, indicating heavy faulting. Moreover, the surface composition of the sample revealed smaller grains and denser twin striations. Due to the chemical connection between C in silicon carbide (SiC) and chlorophyll extracts as 3C-SiC, micro-to-nano-dislocations generate composite flaws. Comparable responses were noted during the production of diverse morphologies of the substance $[CdO_{(75\%)}/VO_{2(20\%)}/SiC_{(4\%)}]$ nanostructures irrespective of the source of C ion was diverse, this is a fair agreement based on the sources used [44].

Figure 5Particle size histograms of the S1 and S2 samples were determined using SEM images as described in the literature [45]. The figure illustrates the particle size distribution of the S1 and S2 samples. S1 has a particle size of 22.64 nm, while S2 has a particle size of 17.85 nm. As the pulse rate rises, there is a significant reduction of around 21%. As a result, the results are consistent with those obtained by the Scherrer method for determining the crystallite size

Granules with assemblage defects are regularly distributed on the film surface due to CdO NPs, VO (II), and SiC accumulation at specific sites without other sites with new growth patterns. In terms of shape and collected togetherness, the particles are regular and irregular on the nanoscale. Since the size of the aggregated particles is semi-uniform, SEM is used to determine the morphology of the particles. The prepared were formed as plate-like aggregates by removing surfactants from the solvothermal process. As shown in Fig. 4a, the product before laser treatment is fused and has an irregular shape. This distinctive structure is of various sizes and shapes and has a hexangular morphology similar to that of a starfruit. It has been reported that specific forms are extensive and are composed of many small particles aggregated together compactly. Alternatively, some structures are comprised

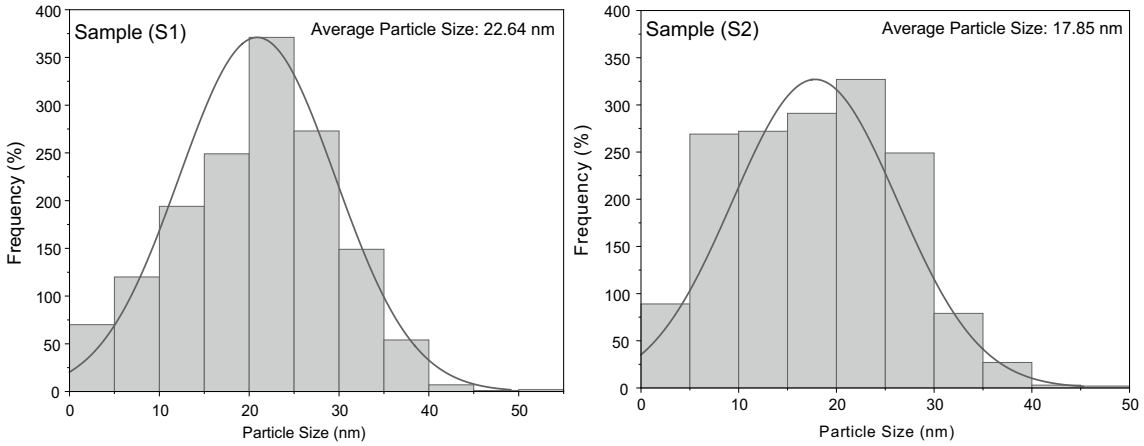

Fig. 5 Particle size histogram of S1 and S2 samples

of only a few particles. The morphology of the products obtained by SEM also shows some single small particles. Tiny holes/pores and little intrinsic spaces can also be observed within any product aggregate. According to Fig. 4b, SEM revealed nano and microparticles in an uneven pattern after laser treatment. Laser treatment (E = 80 mJ and No. of Pulses = 100, 200) compacts the product's particles into nearly spheroids. A regular array of nano and microparticles can be seen in the arrangement of particles, and there are tiny visible spaces between them. When chlorophyll was present before and after laser treatment, these particles did not acquire the shape of flowers. The laser treatment results in the fragmentation of large aggregates, leading to minute nanoparticles in the final product. In agreement with other studies, this study examined whether these particles exhibit an anisotropic morphology. Where it extends from the surface to the inter-particle open spaces, resulting in loosely packed microstructures with sufficient space between them [46].

An XRD pattern is shown in Fig. 6 for the synthesized samples S1 and S2 using the Solvothermal method and treated with Nd: YAG lasers. All diffraction peaks were found to match well with the Standard JCPDS Data Cards for CdO (05–0640), VO_2 (65–7960), SiC (29–1129), and Mg-Chlorophyll (78–0430). Compared with the synthesized composite nanoparticles, the sample exhibited similar diffraction peaks. The porous silica shell shielded the detecting X-rays, resulting in low-intensity retained nanocomposite peaks. Based on XRD patterns, chlorophyll dye-overlaid films have mostly polycrystalline structures, depending on preparation conditions. On glass substrates, an increase in laser energy affects the composition of S2 compared to S1

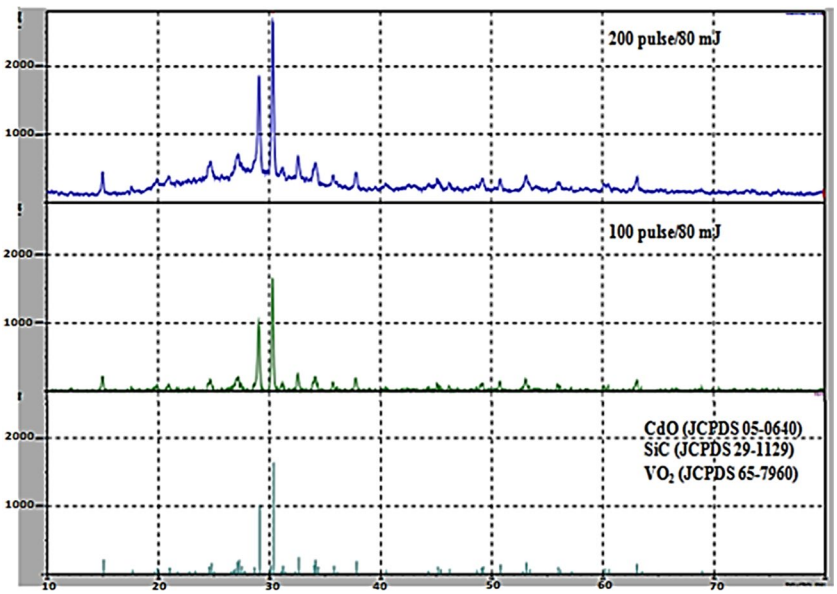

Fig. 6 XRD Pattern of S1 and S2 nanocomposites synthesized compared with JCPDS cards

films. The two numbers have two different pulses (100 and 200 pluses).

According to Fig. 6, when the number of pulses (100 pulses) is the same and sharper and more distinct, respectively, the crystal levels (111) and (002) for CdO and VO_2 become dominant. Increasing laser pulses indicates a polycrystalline film, when the number of laser pulses is increased from 100 to 200, a polycrystalline film is formed. For cadmium and vanadium, other peaks will appear at the diffraction angles for the same oxide. XRD peaks of SiC at (111) and (220) appeared at angles (2θ = 34.1°, 60°), respectively. The diffraction angle (2θ = 34.1°) was observed for Mg at level (111). It is worth mentioning that other researchers have observed similar changes in thin film structure, which indicates a shift toward more stable phases. As a result, VO_2 and SiC have hexagonal crystal structures, while CdO has a cubic crystal structure. The mg-chlorophyll phase was present in the samples and exhibited diffraction peaks similar to the models. The diffraction peaks of both nanocomposites were found to have relatively low intensities [41]. The porous silica exterior is a barrier against X-ray detection [47, 48] in addition to decreasing the chlorophyll concentration and laser pulse number. The grain size increases, as does the dislocation density, which is lower than in non-plasticized thin films. Some levels and faults developed after crystalline grains grew and rearranged at a given temperature for a long time. The SEM analysis has reorganized these defects. Energy is needed for the grains to produce and arrange within the lattice, which means stress is removed. The average particle size decreased from 61.4 nm in S1 to 50.31 nm in S2 when subjected to 80 mJ with a pulse count of 100 and 200. In this test, one can observe that pulse energy affects grain crystallite size. As a result, any amount of silicon carbide or vanadium oxide added increases nucleation centers. Therefore, smaller particle sizes appear. As listed in Table 1, the crystallite size calculations of the synthesized samples were collected using the Debye–Scherrer method [49, 50], as Eq. 2.

$$D = \frac{0.9\lambda}{\beta \cos \theta} \tag{2}$$

Assuming λ is the wavelength of the X-rays, Bragg's angle (θ), and the FWHM (β) in radians of diffracted X-rays.

X-ray Energy Dispersive Measurement can be used to identify the phases of materials present in samples. Figures 6 and 7 show S1 and S2 elements in the synthesized nanocomposites, respectively. A study determined if Cd, V, Si, O, C, and Mg elements were present. In the composite lattice, no VO_2 peaks were detected, which may be related to the substitution of the Cd^{2+}, V^{5+} ions with Mg^{2+} ions due to structural similarities between CdO and SiC. Moreover, no impurities were present in Fig. 6, which indicates that the samples were not contaminated during preparation. In addition, there was no contamination in the testing chamber, as confirmed in Figs. 7 and 8.

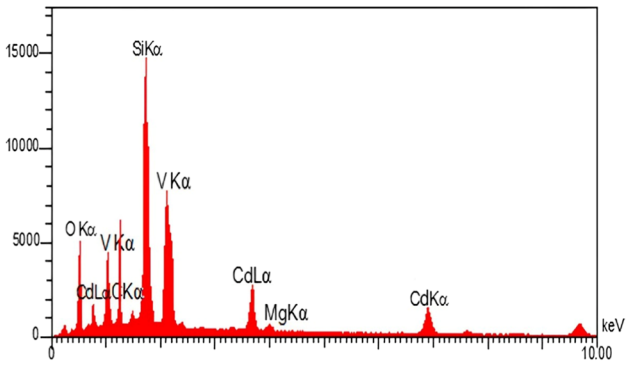

Fig. 7 EDX measurement of synthesized S1 (80 mJ and 100 pulses) nanocomposites

Table 1 EDX data recorded in S1 and S2 synthesized nanocomposite samples

Samples	Physical Quantity	Elements						
		Cd	O	V	Si	C	Mg	Impurities (Au, K, Ca, Al)
S1 [$CdO_{(75\%)}$/ $VO_{2(20\%)}$/ $SiC_{(4\%)}$:p-Si] (80 mJ, 100 Pulses)	Weight%	2.96	1.33	5.78	23.65	5.46	26.33	34.50
	Atomic%	0.85	0.96	2.34	14.87	4.19	38.71	38.08
S2 [$CdO_{(75\%)}$/ $VO_{2(20\%)}$/ $SiC_{(4\%)}$:p-Si] (80 mJ, 200 Pulses)	Weight%	2.96	1.33	8.82	21.71	7.52	24.29	33.37
	Atomic%	0.85	0.96	3.11	13.84	6.42	37.65	37.17

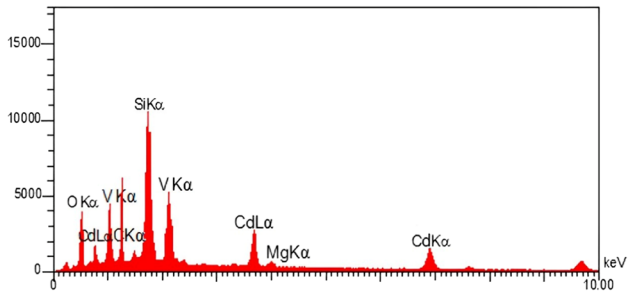

Fig. 8 EDX measurement of synthesized S1 (80 mJ and 200 pulses) nanocomposites

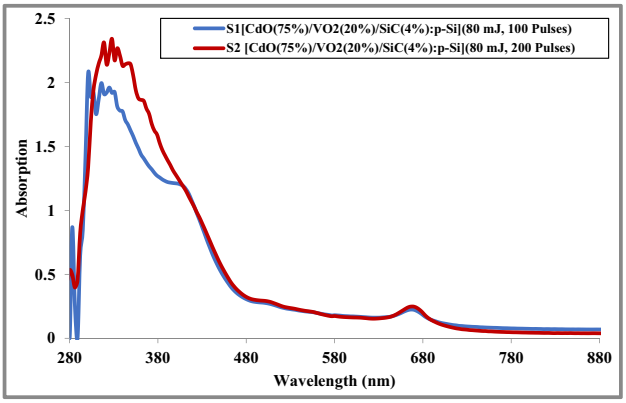

Fig. 9 Absorption Spectrum of the prepared samples S1 and S2

As confirmed by EDX spectroscopy, the composite's elemental composition is solely V, Mg, and C, whose proportions are consistent enough to form nanocomposites. Moreover, the essential mappings of the synthesized composite are described. As a result of solvothermal treatment followed by the Nd: YAG lasing process, the p-Si surface contained a pretty distribution of Cd, V, and Si elements, as listed in Table 1.

UV–Vis. spectrum of S1 and S2 nanocomposites is presented in Fig. 9. At 310 nm and 640 nm, two prominent absorption peaks and three edges at 390 nm for S1 are detected. Artifacts cause band-edge emission at 480 nm for S1 and S2. For two fabricated films synthesized with laser energy 80 mJ, wavelength 1064 nm, frequency 6 Hz, and the number of pulses 100 and 200, the absorbance spectrum changes as a function of wavelength within the range (280–880) nm. It was observed that significant absorbance occurs in the visible region and that it decreases slightly at long wavelengths. In a physical sense, the incident photon could not irritate an electron and transfer it from the valence beam to the conduction beam since the photon energy is less than the energy gap in the semiconductor. At 80 mJ laser energy, the absorbance decreases with increasing wavelength in (nm); at low points, it decreases almost steadily. Several studies have shown that the number of laser pulses impacts the absorbance of synthesized films. When the number of laser pulses is increased, the absorbance emerges in the visible spectrum at a wavelength λ_{max} = 640nm, whereas the most significant number of pulses is 200; the increase in absorbance indicates an increase in granular size and surface roughness. According to their absorbance spectra, both samples contained Cd–O, V–O, Si–O, and Si–C vibrations. The peak at 640 nm in oxide materials is due to an oxygen vacancy with a single ionized electron. Within the valence band, a photogenerated hole recombines with an ionized electron. The transition between the conduction and valence bands is produced at 480 nm. A band at 640 nm is also caused by a near-band gap radiative combination. There is a slight shift to the blue of the absorption edge compared to the absorption edge S1 due to quantum confinements observed with adequate pulse energy. As a result, with increasing pulse counts, the particle size decreases due to particle aggregation due to the formation of dye aggregates around the nanoparticles, corresponding to the measurement of XRD [51, 52].

While keeping the spectral shape constant, there was an increase in the intensity of absorbance. Following the excitation, the spectral shape of the transient absorption spectrum matched that of the long-lasting transient species [53]. Within a laser plume, the collision between electrons and ions occurs as a result of electron–ion interactions. The absorption band expanded into the visible region, making the chlorophyll dye visible. According to the application of nanosecond pulses to nanoparticle films, partially similar peaks were observed. More and more Nd: YAG laser pulses were employed to ablate material-targets. It was determined that the absorption edge at 480 nm was caused by the composition of the thin-film interconnection deposited on Si-Wafers [54].

Following Eqs. 3 and 4, the topic under discussion pertains to the concept of two distinct band gap energies (Eg) associated with Urbach energies (Eu) obtained [27].

$$(\alpha h\nu)^2 = A\left(h\nu - E_g\right) \tag{3}$$

$$(\alpha \nu) = \beta\, e^{(h\nu/Eu)} \tag{4}$$

It is demonstrated that (α) is the absorption coefficient, (hν) is the photon energy, and (A) and (β) are constants that are material-dependent.

Band gap energies of (2.7 eV) and (2.5 eV) are estimated for S1 and S2, respectively. As illustrated in Fig. 10, the valence band degenerates based on the obtained band gap energies. In semiconductor physics, it is essential to understand the optical energy gap. Depending on how semiconductors are used in optical and electronic applications, the value of this constant may vary. Energy gaps are dependent

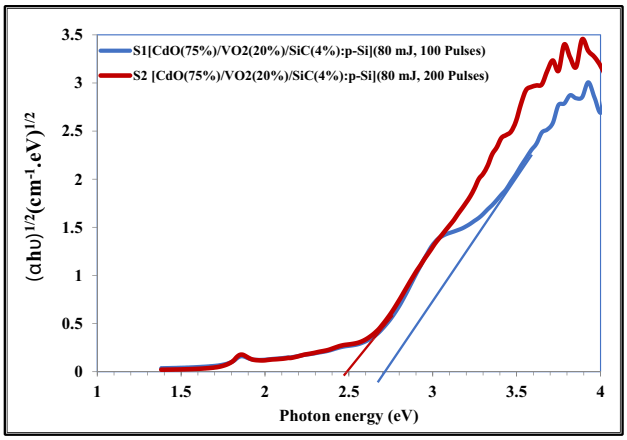

Fig. 10 Photon Energy as a function of $(\alpha h\upsilon)^{1/2}$ for S1 and S2 samples

on crystal structures in a material. Using the absorption coefficient and the energy of the incident photon, the energy gap (E_g) can be determined. Figure 10 determines the permissible energy gap values for S1 and S2 samples. It was found that thin films containing cadmium oxide exhibit increased absorption and absorption coefficients, with an energy gap of 2.15 eV. These band gap energies are lower than those in the literature, possibly due to lattice stretching or nanoparticle size [55].

It is important to note that the particle size of nanoparticles affects their band gap energy. Due to the 'quantum confinement effect the size of the nanoparticles can affect the band gap energy [56]. The lattice parameters increase as the particle size decreases, resulting in more expansive spaces between bands [57]. The band gap increases as the diameter decreases. According to XRD and SEM, the energy gap has also decreased as a result of the decrease in particle size. As nanofilms become smaller, the energy band gap tends to decrease [58]. As a result of a lower band gap, the amount of energy required to excite an electron from the valence band to the conduction band is minimal, and this depends on the size of the nanoparticles. As the size of the device decreases to the nanoscale, electron confinement causes the band gap to increase significantly [59, 60]. The samples show promise for visible-light photocatalytic applications due to the tiny value of the energy gap [61, 62].

5 Current–Voltage Characteristics Measurements at Dark and Illumination

As a method for studying the effects of forward and reverse bias voltage on the current flow. It is widely agreed that the dark I-V characteristic of thin films is a crucial device measuring parameter. Figure 11 shows the fundamental junction diagram of two cells, S1 and S2, produced according to the above mentioned methods.

For about 15–20 min, hydrofluoric acid was sprayed on the silicon wafer slides to etch them. To establish a matrices groove line surface like Fig. 12. Deposition films were mapped out using Teflon masks as electrodes. Note that soft paper was used to dry the samples.

Figure 13 illustrates the I-V characteristics of heterojunction nanocomposites synthesized from S1 and S2 nanocomposites under darkness. According to the figure, the curve exhibits a highly nonlinear characteristic. Thus, it is apparent that the conduction mechanism is non-ohmic and may indicate the existence of multiple conduction mechanisms. When current flows forward through a diode, it has relatively little resistance, while when it flows reversely, it also has relatively little resistance. Most carriers flow at a low current flow, which results in the forward dark present being generated at a deficient flow. By applying voltage, most runners are introduced into the depletion layer, decreasing the width of the depletion layer and the built-in potential. During this recombination, a high majority carrier concentration ($n_i^2 < n_p$) is co-generated with a low voltage region (0–0.3).

The electrons are recombined with holes in the valence band as they move from the valence band to the conduction

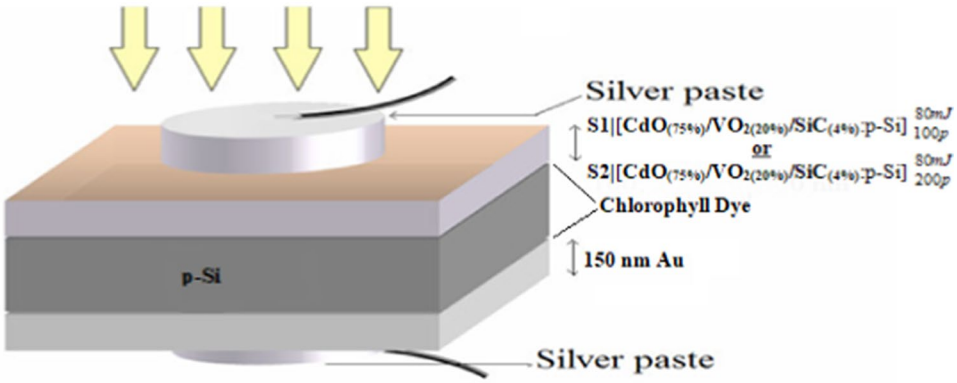

Fig. 11 The fundamental junction diagram of S1 and S2 samples of solar cells

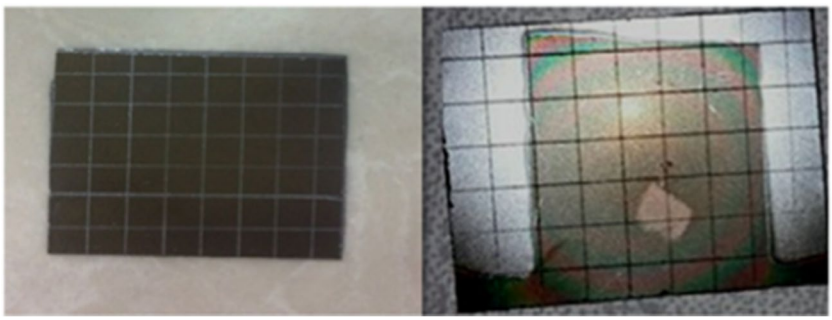

Fig. 12 Silicon Wafer Substrate with matrices grooves

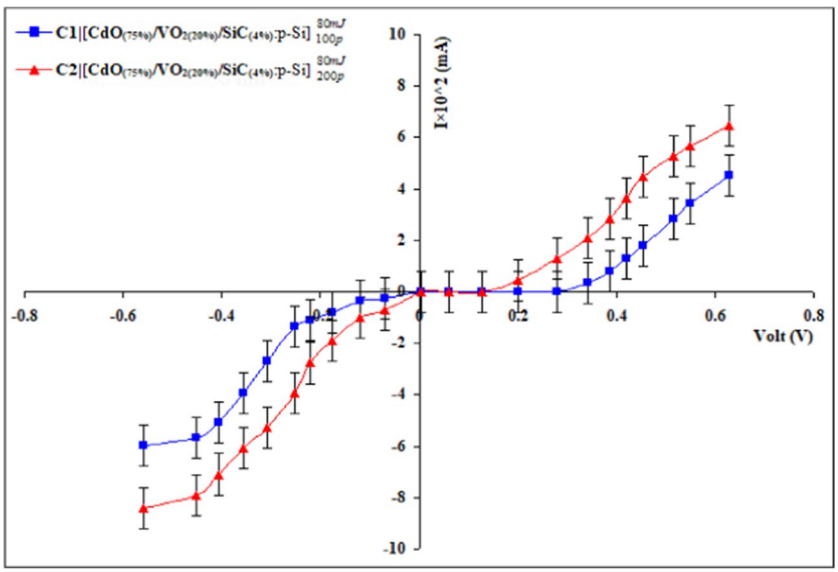

Fig. 13 I-V characteristics under dark for C1 and C2 nanocomposites synthesized heterojunctions

band (C.B). It can be observed that the recombination current is slightly increased at low voltages (0–0.3); high voltages are required for tunneling to occur. As voltage increases, the magnitude of the current increases exponentially. This type is called diffusion current, which dominates at high voltages (above 0.3 V). When reverse bias voltages are applied in the reverse bias region, a broader depletion layer forms, resulting in fewer majority and minority carriers. The reverse bias current has two areas, and the forward bias current has two. Generation currents dominate at low voltages (0.1 Volt), but

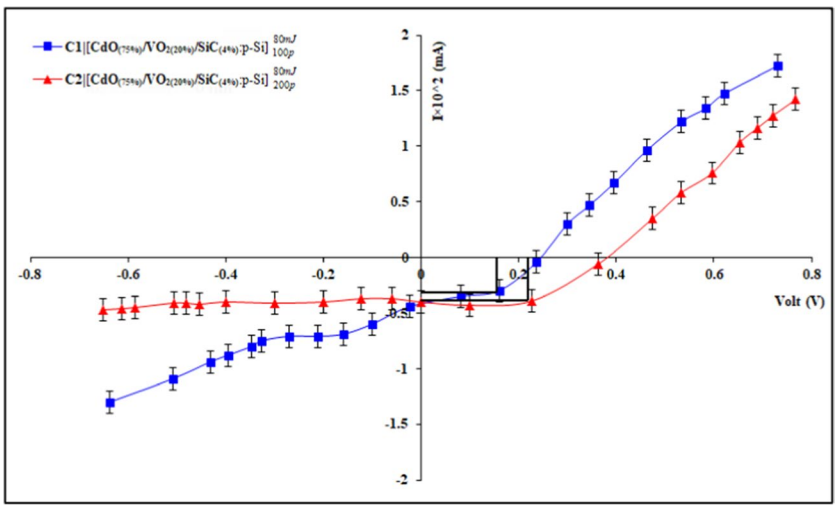

Fig. 14 I-V Characteristics under illumination by (105mW/cm^2) white light for C1 and C2 nanocomposites synthesized heterojunctions

Table 2 I-V parameters for C1 and C2 nanocomposites synthesized heterojunctions under illumination by (105mW/cm^2) white light

Material of Cells	V_{oc} (V)	I_{sc} (mA)	V_m (V)	I_m (mA)	FF	η%
C1: [$CdO_{(75\%)}/VO_{2(20\%)}/SiC_{(4\%)}$:p-Si] (80 mJ, 100 Pulses)	0.31	47	0.195	21.6	0.29	6.79
C2: [$CdO_{(75\%)}/VO_{2(20\%)}/SiC_{(4\%)}$:p-Si] (80 mJ, 200 Pulses)	0.34	40	0.210	32.0	0.48	11.0

diffusion currents are dominant at high voltages (> 0.1 Volt). Increasing laser pulses across heterojunctions S1 and S2, current increases due to increased charge carriers across the junction. As displayed in Fig. 13, recombination currents are located in two regions: tunneling and recombination currents. In this regard, the current forward mechanism coincides.

Two samples of p-Si heterojunctions were synthesized, and their illumination current and voltage relationships are shown in Fig. 13. Measurements were conducted under dual illumination of (105mW/cm^2), with an illuminated cell area of (1.5×2) cm^2. This graph illustrates the photocurrent behavior with forward and reverse bias voltage. According to Fig. 14, When the bias voltage is increased, the photocurrent is increased too. Whereas when the incident power density is increased, the photocurrent increases. As the reverse bias voltage is grown for the heterojunction under illumination, the width of the depletion region increases. Due to the rise in the amount of absorption through it and the formation of electron–hole pairs. The current grows exponentially in forward biasing voltage before leveling out. A high carrier injection level can result in the applied voltage not being fully developed across the depletion region. Figure 14 demonstrates that increased laser pulse count results in a higher photocurrent. Furthermore, it may result from a defect in the interface states. Calculating the fill factor and efficiency from equations down is possible, respectively. I_{SC} and V_{OC} represents the current and voltage in short circuits, respectively. Alternatively, I_m and V_m are the maximum power current and voltage, correspondingly. At that setting, the device's output power is at its highest. The fill Factor is another parameter that comes from Eq. 5 below [63, 64].

$$F.F = V_m I_m / V_{oc} I_{sc} \tag{5}$$

Aspects such as the efficiency of photovoltaic conversion are another critical parameter. Equation 6 provides a formula for determining how much photon energy is transformed into electron energy [65].

$$\eta = \frac{P_m}{P_{in}} = \frac{F.F \times I_{sc} \times V_o}{P_{in}} \times 100\% \tag{6}$$

Where P_m: the area of the maximum power rectangle, P_{in}: the incident power. The I-V parameter values (V_{oc}, I_{sc}, V_{max}, I_{max}, F.F and η) were listed in Table 2.

As concentration increases, short current density increases due to increased absorption of light, as a result of the increased absorbance of photons, the number of photogenerated electrons (charge density) increases, resulting in an increase in current flow. A shift in the Fermi level of electrons in the conduction band of CdO and VO_2 causes an increase in the open circuit voltage, which is explained by the shift in Fermi level of electrons in the conduction band. The increase in open circuit voltage is a result of the shift in the Fermi level of electrons within the conduction band of oxide materials. Equation (5) demonstrates that a silicon solar cell has the potential to produce a maximum open circuit voltage. Recombination losses, on the other hand, lead to a decrease in the open circuit voltage. The number of chain groups that adhere to chlorophyll surfaces and the chemical reactions involving oxide groups in materials both influence the Fermi level. As the concentration increases, the I-V curves become closer together due to the saturation of both the short circuit current and open circuit voltage. Due to changes in the conduction band, the properties of the material oxides utilized in the fabrication of solar cells, along with the size of nanofilms, lead to a reduction in the efficiency of electron injection into the conduction band of CdO and VO_2 with SiC. The arrangement of carbon chains affects how the chlorophyll molecules bind to the surface of the composite. This impacts the charge injection into the conduction band of CdO and VO_2 with SiC, along with the Fermi level of electrons in the band gap. Understanding the connection between short circuit current and open circuit voltage is crucial in determining the fill factor and solar conversion efficiency. Variations in open circuit voltage and short circuit current are the cause of their changes [66].

6 Conclusions

A wet chemical synthesis method named solvothermal technique was successfully employed to synthesize [$CdO_{(75\%)}/VO_{2(20\%)}/SiC_{(4\%)}$]. Nd: YAG lasers were used to treat the prepared nanocomposite samples (1064 nm, 80 mJ, at pulse counts 100 and 200). According to the results, grain size decreased with the addition of vanadium oxide. At the same time, it increased at low energy levels and low chlorophyll concentration. Although dislocation density was lower than in the non-plasticized thin films, it was still more significant than in the non-plasticized thin films. After grain growth and rearrangement, deposition at a specific temperature for extended periods

reconfigured several levels and flaws. In the present study, synthesized films grew in a hexagonal wurtzite structure. Before and after laser treatment, substantial changes were observed in particle morphology, size, and arrangement SEM. After laser treatment, morphology is considerably looser but sequentially arranged compared to morphology obtained before. It was found that the synthesized product could be thermally decomposed when used as a catalyst. There was a significant reduction in thermal degradation when $[CdO_{(75\%)}/VO_{2(20\%)}/SiC_{(4\%)} : p - Si]$ nano aggregates were used as a catalyst for laser thermal decomposition. The flash point and fire point have been reduced to facilitate burning. Consequently, the synthesized product is well suited to use as a catalyst, fuel additive, and solar cell, where its efficiency was improved ($\eta = 6.79\%$ to 11%). Using an Nd: YAG laser, this study used two different laser pulse rates at an energy of 80 mJ to prepare thin CdO/VO (II) thin films. A 30 to 70 percent percentage weight was recommended for S1 and S2 sample preparation.

Acknowledgements The authors would like to thank the University of Babylon and Al-Mustaqbal University, Iraq.

Author Contributions Ammar Abd Ali Najm and Zaid L. Hadi designed the idea and experimental part. Saif M. Alshrefi prepared the samples and wrote the introduction, laser process, and experimental sections. Ehssan Al-Bermany performed an analysis of the SEM and optical properties. Zaid L. Hadi contributed to the electrical properties. Ammar Abd Ali contributed to the XRD and I-V tests and wrote the conclusions. Saif M. Alshrefi and Ameen Alwan Mohaimeed contributed to the histogram of SEM images of grain distribution and I-V results. All authors read and approved the final submission.

Funding Not applicable.

Data Availability No datasets were generated or analysed during the current study.

Declarations

Ethical Approval Not applicable.

Consent to Participate Not applicable.

Consent for Publication Not applicable.

Competing Interests The authors declare no competing interests.

References

1. Semaltianos NG (2010) Nanoparticles by laser ablation. Crit Rev Solid State Mater Sci 35:105–124. https://doi.org/10.1080/10408431003788233
2. Al-Bermany E, Chen B (2023) Effect of the functional groups of polymers on their adsorption behavior on graphene oxide nanosheets. Macromol Chem Phys 224:2300101. https://doi.org/10.1002/macp.202300101
3. Al Nafiey A, Addad A, Sieber B et al (2017) Reduced graphene oxide decorated with Co3O4 nanoparticles (rGO-Co3O4) nanocomposite: a reusable catalyst for highly efficient reduction of 4-nitrophenol, and Cr(VI) and dye removal from aqueous solutions. Chem Eng J 322:375–384. https://doi.org/10.1016/j.cej.2017.04.039
4. Elazab HA, Moussa S, Gupton BF, El-Shall MS (2014) Microwave-assisted synthesis of Pd nanoparticles supported on Fe3O4, Co3O4, and Ni(OH)2 nanoplates and catalysis application for CO oxidation. J Nanoparticle Res 16:2477. https://doi.org/10.1007/s11051-014-2477-0
5. Jamil S, Janjua MRSA, Khan SR (2017) Synthesis of Self-assembled Co3O4 nanoparticles with porous sea urchin-like morphology and their catalytic and electrochemical applications. Aust J Chem 70:908–916. https://doi.org/10.1071/CH16694
6. Jamil S, Janjua MRSA, Khan SR (2018) Synthesis and structural investigation of polyhedron Co3O4 nanoparticles: Catalytic application and as fuel additive. Mater Chem Phys 216:82–92. https://doi.org/10.1016/j.matchemphys.2018.05.051
7. Li J, Yang Z, Qiu H et al (2013) Microwave-assisted simultaneous reduction and titanate treatment of graphene oxide. J Mater Chem A 1:11451–11456. https://doi.org/10.1039/c3ta12228j
8. Obaid AN, Al-Bermany E (2023) Performance of functionalized graphene oxide to improve anti-corrosion of epoxy coating on 2024–T3 aluminium alloy. Mater Chem Phys 305:127849. https://doi.org/10.1016/j.matchemphys.2023.127849
9. Nie M, Sun K, Meng DD (2009) Formation of metal nanoparticles by short-distance sputter deposition in a reactive ion etching chamber. J Appl Phys 106:054314. https://doi.org/10.1063/1.3211326
10. Shaker SS, Ismail RA, Mohammed BK (2023) Preparation of graphene oxide@ZrO2 core/shell nanoparticles by two-step laser ablation in liquid towards a high-performance silicon-based heterojunction photodetector. Silicon 15:5791–5802. https://doi.org/10.1007/s12633-023-02476-6
11. Gubin SP, Koksharov YA, Khomutov GB, Yurkov GY (2005) Magnetic nanoparticles: preparation, structure and properties. Usp Khim 74:539–574. https://doi.org/10.1070/rc2005v074n06abeh000897
12. Jasim SA, Banimuslem HAJ, Alsultany FH et al (2023) Ammonia and nitrogen dioxide detection using ZnO/CNT nanocomposite synthesized by sol–gel technique. J Sol-Gel Sci Technol 108:734–741. https://doi.org/10.1007/s10971-023-06190-y
13. Al-Bermany E, Mekhalif AT, Banimuslem HA et al (2023) Effect of green synthesis bimetallic Ag@SiO2 core–shell nanoparticles on absorption behavior and electrical properties of PVA-PEO nanocomposites for optoelectronic applications. Silicon. https://doi.org/10.1007/s12633-023-02332-7
14. Abdulridha AR, Al-Bermany E, Hashim FS, Omran Alkhayatt AH (2020) Synthesis and characterization and pelletization pressure effect on the properties of Bi1.7Pb0.3Sr2W0.2 Ca2Cu3 O10+δ superconductor system. Intermetallics 127:106967. https://doi.org/10.1016/j.intermet.2020.106967
15. Vadgama VS, Vyas RP, Jogiya BV, Joshi MJ (2017) Synthesis and characterization of CdO nano particles by the sol-gel method. AIP Conf Proc 1837:040016. https://doi.org/10.1063/1.4982100
16. Thema FT, Beukes P, Gurib-Fakim A, Maaza M (2015) Green synthesis of Monteponite CdO nanoparticles by Agathosma betulina natural extract. J Alloys Compd 646:1043–1048. https://doi.org/10.1016/j.jallcom.2015.05.279
17. Milošević S, Stojković I, Kurko S et al (2012) The simple one-step solvothermal synthesis of nanostructurated VO 2(B). Ceram Int 38:2313–2317. https://doi.org/10.1016/j.ceramint.2011.11.001
18. Devthade V, Lee S (2020) Synthesis of vanadium dioxide thin films and nanostructures. J Appl Phys 128:231101. https://doi.org/10.1063/5.0027690
19. Cheng H, Yang M, Lai Y et al (2018) Transparent highly oriented 3C-SiC bulks by halide laser CVD. J Eur Ceram Soc

38:3057–3063. https://doi.org/10.1016/j.jeurceramsoc.2018.03.015
20. Ceballos-Mendivil LG, Cabanillas-López RE, Tánori-Córdova JC et al (2014) Synthesis and characterization of silicon carbide in the application of high temperature solar surface receptors. Energy Procedia 57:533–540. https://doi.org/10.1016/j.egypro.2014.10.207
21. Kannan CR, Manivannan S, Stalin B, Kailasanathan C (2022) Metallographic characterization of SiC-Ni-Ti layer reinforced on austenitic stainless steel (AISI 316L) by two-step laser fabrication. Silicon 14:5393–5400. https://doi.org/10.1007/s12633-021-01305-y
22. Omar MK, Ahmed NM, Alqanoo AAM et al (2024) Performance evaluation of aluminum nitride-decorated AgNWs-based transparent conductive electrodes deposited on flexible substrates. J Mater Sci Mater Electron 35:436. https://doi.org/10.1007/s10854-024-12211-5
23. De Lezaeta M, Lam M, Black S et al (2005) The synthesis of III-V semiconductor insb nanoparticles by solvothermal reduction reactions. Mater Res Soc Symp Proc 848:189–193. https://doi.org/10.1557/proc-848-ff3.34
24. Duta L, Popescu AC (2021) Current research in pulsed laser deposition. Coatings 11:1–5. https://doi.org/10.3390/coatings11030274
25. Zhang J, Zhong A, Huang G et al (2020) Enhanced efficiency with CDCA co-adsorption for dye-sensitized solar cells based on metallosalophen complexes. Sol Energy 209:316–324. https://doi.org/10.1016/j.solener.2020.08.096
26. Yakuphanoglu F (2010) Nanocluster n-CdO thin film by sol-gel for solar cell applications. Appl Surf Sci 257:1413–1419. https://doi.org/10.1016/j.apsusc.2010.08.045
27. Alawi AI, Al-Bermany E (2023) Newly fabricated ternary PAAm-PVA-PVP blend polymer doped by SiO2: absorption and dielectric characteristics for solar cell applications and antibacterial activity. Silicon. https://doi.org/10.1007/s12633-023-02477-5
28. Koifman OI, Stuzhin PA, Travkin VV, Pakhomov GL (2021) Chlorophylls in thin-film photovoltaic cells, a critical review. RSC Adv 11:15131–15152. https://doi.org/10.1039/d1ra01508g
29. Ashokkumar K, Selvaraj K, Muthukrishnan SD (2013) Cynodon dactylon (L.) Pers.: an updated review of its phytochemistry and pharmacology. J Med Plants Res 7:3477–3483. https://doi.org/10.5897/JMPR2013.5316x
30. Prakash S (1975) Advanced chemistry of rare earth, 3rd ed. Chemical Publishing Company
31. Ramsay W, Ramsay W (1891) A System of Inorganic Chemistry. Nature 44:50–51. https://doi.org/10.1038/044050a0
32. Neiner D, Chiu HW, Kauzlarich SM (2006) Low-temperature solution route to macroscopic amounts of hydrogen terminated silicon nanoparticles. J Am Chem Soc 128:11016–11017. https://doi.org/10.1021/ja064177q
33. Lan Y, Minnich AJ, Chen G, Ren Z (2010) Enhancement of thermoelectric figure-of-merit by a bulk nanostructuring approach. Adv Funct Mater 20:357–376. https://doi.org/10.1002/adfm.200901512
34. Liang S, Li L (2018) Improved thermoelectric performance of CdO by adding SiC fibers versus by adding SiC nanoparticles inclusions. J Appl Phys 123:114303. https://doi.org/10.1063/1.5012046
35. Maestre D, Cremades A, Piqueras J (2005) Growth and luminescence properties of micro- and nanotubes in sintered tin oxide. J Appl Phys 97:044316. https://doi.org/10.1063/1.1851602
36. Sindhu S, Anantharaman MR, Thampi BP et al (2002) Evaluation of a.c. conductivity of rubber ferrite composites from dielectric measurements. Bull Mater Sci 25:599–607. https://doi.org/10.1007/BF02707892
37. Alivisatos A (2003) Hybrid nanorod-polymer solar cell hybrid nanorod-polymer solar cell final report. Natl Renew Energy Lab 89:9
38. Du Pasquier A, Chen H, Lu Y (2006) Dye sensitized solar cells using well-aligned zinc oxide nanotip arrays. Appl Phys Lett 89:1–4. https://doi.org/10.1063/1.2420779
39. Lanje A, Satish Sharma RP (2014) Functional Nanomaterial Synthesis and Characterization Electrical, Magnetic and Optical. LAP Lambert Academic Publishing, Deutscland, Germany, pp 54–121
40. Tadeo IJ, Bhardwaj D, Sheela D et al (2020) Highly photoresponsive VO2(M1) thin films synthesized by DC reactive sputtering. J Mater Sci Mater Electron 31:4687–4695. https://doi.org/10.1007/s10854-020-03023-4
41. Gangwar J, Gupta BK, Srivastava AK (2016) Prospects of emerging engineered oxide nanomaterials and their applications. Def Sci J 66:323–340. https://doi.org/10.14429/dsj.66.10206
42. Fiedor L, Stąsiek M, Myśliwa-Kurdziel B, Strzałka K (2003) Phytol as one of the determinants of chlorophyll interactions in solution. Photosynth Res 78:47–57.https://doi.org/10.1023/A:1026042005536
43. Ashcroft SP, Stocks B, Egan B, Zierath JR (2024) Exercise induces tissue-specific adaptations to enhance cardiometabolic health. Cell Metab 36:278–300. https://doi.org/10.1016/j.cmet.2023.12.008
44. Otgonbayar Z, Jun Joo Y, Youn Cho K et al (2022) Novel preparation of functional β-SiC fiber based In2O3 nanocomposite and controlling of influence factors for the chemical gas sensing. Sci Rep 12:1–16. https://doi.org/10.1038/s41598-022-11000-6
45. Arefi-Rad MR, Kafashan H (2020) Pb-doped SnS nano-powders: Comprehensive physical characterizations. Opt Mater (Amst) 105:109887. https://doi.org/10.1016/j.optmat.2020.109887
46. Chander S, Tripathi SK (2022) Recent advancement in efficient metal oxide-based flexible perovskite solar cells: a short review. Mater Adv 3:7198–7211. https://doi.org/10.1039/d2ma00700b
47. Zhu Y, Mendelsberg RJ, Zhu J et al (2013) Structural, optical, and electrical properties of indium-doped cadmium oxide films prepared by pulsed filtered cathodic arc deposition. J Mater Sci 48:3789–3797. https://doi.org/10.1007/s10853-013-7179-y
48. Çolak H, Türkoğlu O (2013) Synthesis and characterization of Fe-doped CdO binary system. J Ceram Process Res 14:616–622
49. Morelhão SL, Kycia SW, Vartaniants IA (2022) A simple formula for determining nanoparticle size distribution by combining small-angle X-ray scattering and diffraction results. Acta Crystallogr Sect A Found Adv 78:459–462
50. FadhlAbodood AA, Abdali K, Mousa Al-Ogaili AO et al (2023) Effect of molar concentration and solvent type on linear and NLO properties of Aurintricarboxylic (ATA) organic dye for image sensor and optical limiter applications. Int J Nanosci 22:22–23. https://doi.org/10.1142/S0219581X2350014X
51. Reddy SR, Prasad R, Sharan A, Prasad B (2013) Development of laser edge isolation process for industrial solar cells. Int J Innov Res Sci Eng Technol 2:5780–5785
52. Jabbar SA, Khalil SM, Abdulridha AR et al (2022) Dielectric, AC conductivity and optical characterizations of (PVA-PEG) doped SrO hybrid nanocomposites. Key Eng Mater 936:83–92. https://doi.org/10.4028/p-41a757
53. Aldulaimi NR, Al-Bermany E (2022) Tuning the bandgap and absorption behaviour of the newly-fabricated ultrahigh molecular weight polyethylene oxide- polyvinyl alcohol/ graphene oxide hybrid nanocomposites. Polym Polym Compos 30:096739112211121. https://doi.org/10.1177/09673911221112196
54. Huda Abdul Razak N, Amin N, Sajedur Rahman K et al (2023) Influence of pulsed Nd:YAG laser oscillation energy on silicon wafer texturing for enhanced absorption in photovoltaic cells. Results Phys 48:106435. https://doi.org/10.1016/j.rinp.2023.106435
55. Tuama AN, Al-Bermany E, Alnayli RS, et al (2024) A critical review of the evaluation of Sio2-incorporated Tio2 nanocomposite for photocatalytic activity. Silicon. https://doi.org/10.1007/s12633-024-02870-8

56. Jawad ED, Khudhair SH, Ali HN (2011) A thermodynamic study of adsorption of some days on Iraqi Bentoniet modified clay. Eur J Sci Res 60:63–70
57. Abdali K, Abass KH, Al-Bermany E et al (2022) Morphological, optical, electrical characterizations and Anti- Escherichia coli Bacterial Efficiency (AECBE) of PVA/PAAm/PEO polymer blend doped with silver NPs. Nano Biomed Eng 14:114–122. https://doi.org/10.5101/nbe.v14i2.p114-122
58. Ghazi RA, Al-Mayalee KH, Al-Bermany E et al (2022) Impact of polymer molecular weights and graphene nanosheets on fabricated PVA-PEG/GO nanocomposites: morphology, sorption behavior and shielding application. AIMS Mater Sci 9:584–603. https://doi.org/10.3934/matersci.2022035
59. Kafashan H, Rabiei Baboukani A (2024) Electrochemically deposited nanostructured Cd-doped SnS thin films: Structural and optical characterizations. Ceram Int 50:5717–5727. https://doi.org/10.1016/j.ceramint.2023.11.354
60. Kafashan H, Orshesh Z, Bahrami A, Zakerian F (2024) Structural and optoelectronic properties of electrodeposited CdSe thin films: effect of Cu-dopant. Phys B Condens Matter 675:415623. https://doi.org/10.1016/j.physb.2023.415623
61. Al Boukhari J, Zeidan L, Khalaf A, Awad R (2019) Synthesis, characterization, optical and magnetic properties of pure and Mn, Fe and Zn doped NiO nanoparticles. Chem Phys 516:116–124. https://doi.org/10.1016/j.chemphys.2018.07.046
62. Alawi AI, Al-Bermany E, Alnayli RS et al (2024) Impact of SiO2–GO hybrid nanomaterials on opto-electronic behavior for novel glass quinary (PAAm–PVP–PVA/SiO2–GO) hybrid nanocomposite for antibacterial activity and shielding applications. Opt Quantum Electron 56:429. https://doi.org/10.1007/s11082-023-06070-3
63. Zhu M, Qi H, Li C et al (2018) VO2 thin films with low phase transition temperature grown on ZnO/glass by applying substrate DC bias at low temperature of 250 °C. Appl Surf Sci 453:23–30. https://doi.org/10.1016/j.apsusc.2018.05.089
64. Al-Mamoori MHK, Alshrefi SM, Jader MJ, Kodeary AK (2020) Structural characteristics, synthesis of novel TiO2/VO (II) composites thin films decorated with chlorophyllvia solvothermal-laser dual technique. NeuroQuantology 18:6–15. https://doi.org/10.14704/nq.2020.18.3.NQ20144
65. Sze SM, Mattis DC (1970) Physics of semiconductor devices. Phys Today 23:75–75. https://doi.org/10.1063/1.3022205
66. Amogne NY, Ayele DW, Tsigie YA (2020) Recent advances in anthocyanin dyes extracted from plants for dye sensitized solar cell. Mater Renew Sustain Energy 9:23. https://doi.org/10.1007/s40243-020-00183-5